Early Stage Melt Ejection in Percussion Laser Drilling

Tom A. Eppes[*1], Ivana Milanovic[1], and Harini Patlolla[1]
[1]University of Hartford
*200 Bloomfield Ave., West Hartford, CT, USA 06117, eppes@hartford.edu

Abstract: Laser percussion drilling is widely used in the aerospace industry to produce cooling holes in jet engine components. This process is a thermal, contact-free process which involves firing a sequence of focused optical pulses onto a target material. During each optical pulse, the central portion of the target area heats to a liquid then vapor state where the expanding gas produces a recoil pressure that forces the liquid material to move outward and upward in a conical fashion. This paper presents a 2-D, time-dependent analysis of laser percussion drilling that focuses on the early stage of melt formation and ejection using a non-isothermal laminar flow model using COMSOL Multiphysics® 4.3.

Keywords: laser drilling, percussion, melt ejection, evaporation.

1. Introduction

This paper presents a 2-D, time-dependent analysis of laser percussion drilling that focuses on the early stage of melt formation and ejection. The non-isothermal laminar flow (nitf) physics interface is the basis for the model that also includes the angle of incidence and optical intensity profile (Gaussian and flat-top). The target material is iron with temperature dependent material properties to enable the phase transitions. The basis for the work lies in developing a better model for laser hole drilling of aerospace turbo-machinery components.

Cooling holes are used in a variety of jet engine components and may be manufactured using several methods. Conventional mechanical drilling, electric discharge machining (EDM), electrochemical drilling (ECD) and electron beam drilling (EBD) are limited to the particular type of material, suffer from the tool wear, high cost of consumables and long production time. Laser drilling is a thermal, contact-free process that utilizes a focused laser beam to remove material by vaporization and/or melt ejection.

The two leading laser techniques for producing holes are trepanning and percussion drilling. Trepanning is a faster and more efficient for drilling large holes. Percussion drilling is better suited to small holes since laser beams can be focused to small spot sizes thereby creating large concentrations of incident energy. Percussion laser drilling has been successfully used in manufacturing for a number of years in components such as turbine blades, fans, rings, baseplates and afterburners.

Developing an accurate theoretical model for the percussion drilling process is a daunting challenge. The collective integration of the thermal, fluid, optical, electromagnetic, chemical, metallurgical and kinetic effects must be considered. Some relevant models that predict laser drilling outcomes have been developed. Ready's one-dimensional model assumed that material was removed by evaporation only [1]. An additional mechanism of material removal was suggested by Von Allmen [2]. As a result of surface evaporation, vapor is pushed away from the surface. Semak et al. [3] introduced more accurate calculation of melt front dynamics, and this allowed for a two-dimensional evaporation laser drilling model capable of predicting temperature fields by Patel et al. [4]. The recoil pressure removal mechanism was shown to become important with lower absorbed beam intensities or longer interaction times.

Low et al. [5] developed an improved one-dimensional hydrodynamic model incorporating the effect of oxygen as an assist gas. Results from Ref. [5] indicated that recoil pressure at low absorbed laser intensities considerably influenced melt ejection. This was followed by a refined hydrodynamic model reported by Ng et al. [6]. Based on the analytical model from Ref. [6], the authors created a desktop modeling utility that could be used outside large computational environments [7].

2. Governing Equations & Constraints

The model reported in this paper uses the non-isothermal flow interface which includes conductive, convective and heat transfer by

radiation. The governing equations are given in Eqns. 1-3 below.

$$\rho\frac{\partial u}{\partial t}+\rho(u\cdot\nabla)u=\nabla\cdot[-pI+\mu(\nabla u+(\nabla u)'-\frac{2}{3}\mu(\nabla\cdot u)I]+F \quad (1$$

$$\frac{\partial\rho}{\partial t}+\nabla\cdot(\rho u)=0 \quad (2$$

$$\rho C_p\frac{\partial T}{\partial t}+\rho C_p u\nabla T=\nabla\cdot(k\nabla T)+Q \quad (3$$

where u = velocity vector (m/s)
p = pressure (Pa)
ρ = density (kg/m^3)
μ = dynamic viscosity (Pa-s)
F = body force (gravity) (N/m^3)
C_p = specific heat (J/kg-K)
T = absolute temperature (K)
k = thermal conductivity
Q = incident heat source (W/m^2)

The radiation in participating media sub-node is made activate with scattering coefficients set to 0 for both the air and iron regions. The absorption coefficients are set to 0.0 for the air and 1000m^{-1} (essentially opaque) for iron.

3. Parameters, Geometry & Mesh

The geometry consists of a simple 2-D structure with one rectangular domain of air. A second rectangular domain represents the target material and is located beneath the air. The dimensions of the two regions are provided in Table 1.

Table 1: Physical dimensions of regions.

Region	Width (mm)	Height (mm)
Air	3	6
Target	3	3

The model contains two possible optical beam profiles: Gaussian and flat-top. Values for the intensity as a function of position along the surface of incidence and overall beam width are computed in a variables sub-node. The angle of incidence may be varied from 0°-90° so that absorbed optical power can be calculated. In addition, the polarization may be designated as either parallel or normal to the plane of incidence. The output power level of the laser output is also set in the variable sub-node.

The material properties of the air are obtained directly from the COMSOL model library. The properties of iron are temperature dependent and have transitions built into them to reflect the phase changes of solid-to-liquid and subsequently to vapor. Table 2 shows the parameters and expressions used.

Table 2: Key parameters in the model.

Parameter	Description	Expression
n (iron)	Index of refraction (real)	3.12
k (iron)	Index of refraction (imag)	4.26
Po	Optical power	800 W
beam_size	Laser beam width	500 µm
θ	Incidence angle	0-90 degrees
pulse_width	Target beam width	
$\frac{beam\_size}{\cos\theta}$		
w	Half-beam width	Pulse_width/2
Area	Effective area on target	
$\pi w\frac{beam\_size}{4}$		
Area2	Area of flat top ellipse on target	
$\pi w\frac{beam\_size}{2}$		
A	Intermediate variable	
$\sqrt{1+\left(\frac{\sin^2\theta}{n^2+k^2}\right)^2-\frac{4n^2}{n^2+k^2}\frac{\sin^2\theta}{n^2+k^2}}$		
B	Intermediate variable	
$\sqrt{\frac{n^2+k^2}{2n^2}\cdot\frac{n^2-k^2}{n^2+k^2}-\frac{\sin^2\theta}{n^2+k^2}+A}$		
G	Intermediate variable	
$\frac{n^2-k^2}{n^2+k^2}B+\frac{2nk}{n^2+k^2}\sqrt{\frac{n^2+k^2}{n^2}A-B^2}$		
rhoper	Reflection coefficient (perpendicular)	
$\left[\left(nB-\cos^2\theta\right)+\left(n^2+k^2\right)A\right]-\frac{n^2B^2}{\left(nB+\cos\theta\right)^2}+\left(n^2+k^2\right)A-n^2B^2$		

rhoparl	Reflection coefficient (parallel)
$nG-\left(\frac{A}{\cos\theta}\right)^2+\left(n^2+k^2\right)A-\frac{n^2G^2}{nG+\left(\frac{A}{\cos\theta}\right)^2}+\left(n^2+k^2\right)A-n^2G^2A-n^2G^2$	
Igauss_per	Intensity Gaussian (perpendicular)
$\left(Po\frac{1-rhoper}{Area}\right)\exp\left(-2\left(\frac{x}{w}\right)^2\right)$	
Igauss_parl	Intensity Gaussian (parallel)
$\left(Po\frac{1-rhoper1}{Area}\right)\exp\left(-2\left(\frac{x}{w}\right)^2\right)$	
IFT_per	Intensity flat top (perpendicular)
$\left(Po\frac{1-rhoper}{Area2}\right)\left[flc2hs\left(x+\frac{pulse\_width}{2.2e-5}\right)-flc2hs\left(x-\frac{pulse\_width}{2.2e-5}\right)\right]$	
IFT_parl	Intensity flat top (parallel)
$\left(Po\frac{1-rhoper1}{Area2}\right)\left[flc2hs\left(x+\frac{pulse\_width}{2.2e-5}\right)-flc2hs\left(x-\frac{pulse\_width}{2.2e-5}\right)\right]$	

Table 3 shows other properties associated with iron. The thermal conductivity and ratio of specific heat is held constant throughout the process. Four parameters set the initial temperature as well as phase change event temperatures and latent heats.

Table 3: Key temperature related parameters.

Parameter	**Value**
Thermal conductivity (k)	76.2 W/mK
Ratio of specific heat (γ)	1.4
Initial temperature (T_0)	300K
Melting temperature (T_m)	1,808K
Vaporization temperature (T_v)	3,100K
Phase change transition range (dT)	50K
Latent heat of melt (dH_m)	247 kJ/kg
Latent heat of vaporization (dH_v)	6088 kJ/kg

Table 4 shows the expressions that calculate the temperature dependent iron properties for density, dynamic viscosity and specific heat. Heaviside functions are used in the transition regions for the latent heats of melt and vaporization so the discretization is continuous.

Table 4: Material properties of iron.

Iron Property	**Expression**
C_{p_melt}	Latent heat of melt
$\left(611\frac{J}{kgK}-460\frac{J}{kgK}\right)flc2hs\left(T-T_m,dT\right)+\frac{dH_m\frac{J}{kg}}{\sqrt{\pi dT^2}}\exp\left[-\frac{\left(T-T_m\right)^2}{dT^2}\right]$	
C_{p_vap}	Latent heat of vaporization
$\left(611\frac{J}{kgK}-460\frac{J}{kgK}\right)flc2hs\left(T-T_v,dT\right)+\frac{dH_m\frac{J}{kg}}{\sqrt{\pi dT^2}}\exp\left[-\frac{\left(T-T_v\right)^2}{dT^2}\right]$	
C_{p1}	Specific heat
460[J/kgK] + C_{p_melt} + C_{p_vap}	
R	8.314 J/K-mol
M	0.05584 kg/mol
R_{spec}	R/M J/Kkg
Density (iron_rho) $\rho\left(\frac{kg}{m^3}\right)$	$7870\left[1-flc2hs\left(T-T_v,100\right)\right]+\frac{p}{R_{spec}T}$
Dynamic Viscosity (iron_mu) $\mu\left(Pa\cdot s\right)$	$1-0.994\,flc2hs\left(T-T_m,100\right)$

Several thermal and fluid boundary conditions are imposed. An insulation boundary is applied to the two vertical and horizontals walls of the iron region. The three boundaries surrounding the air region are set to a constant 300K temperature. For radiation purposes, all six walls are set to opaque with an emissivity equal to zero. From a fluid perspective, these same six walls are set to a 'slip' condition. A volume force equal to $-g_{const}nitf.rho$ accounts for gravity in the negative y-direction. The optical energy is

coupled using an incident intensity sub-node set to Iguass_per for this study.

The mesh is divided into two regions. The upper region is constructed of fine elements and encompasses the air as well as a portion of the target to a depth of 1mm. The second region contains coarser elements and consists of that portion of the target below 1mm. As shown in Fig. 2, the overall mesh totals 15,214 triangular elements with an average quality of 99%.

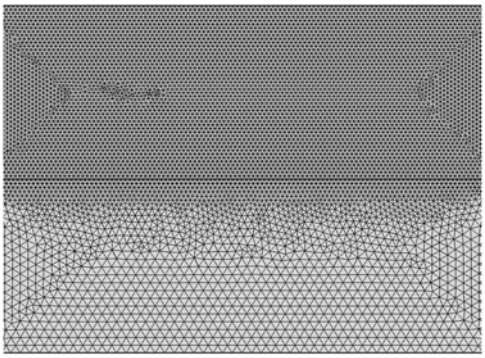

Figure 1. Mesh and size distribution.

4. Results

This paper focusses on the early stages of melt ejection; consequently, only a Gaussian beam profile incident normal to the target is investigated. A time dependent study starting at t=0 with a target material initial temperature of 300K is presented. Early in the process and as the iron heats above 1,000K, a convective air flow pattern begins to form directly above the area of illumination. Once the melting temperature is reached, the model transitions the iron's specific heat to account for the phase change from solid-to-liquid. The viscosity is reduced to that of liquid iron to allow fluid flow to occur as the melt pool of iron begins to form.

At t=2msec, a small portion of the iron reaches the vaporization temperature. The material properties are again transitioned over a 50K range to that of vaporized iron. The viscosity is significantly affected, and the ideal gas law is used to compute density as a function of the instantaneous pressure. It is at this point that the drilling process becomes more dynamic. A force component provided by the expanding iron vapor appears along the surface of the melt pool. Figure 2 shows the temperature 2msec after the optical pulse begins and soon after the vaporization point is reached. A significant plume develops from the target surface rising upward into the surrounding air.

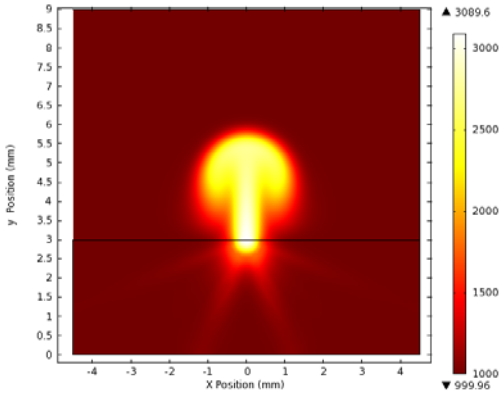

Figure 2. Temperature at t=2 msec.

Figure 3 shows the velocity field at the same instant of time. The primary direction is vertical with a maximum speed of 66m/sec. The shape of the velocity field is similar to a column rising directly above the laser incidence region.

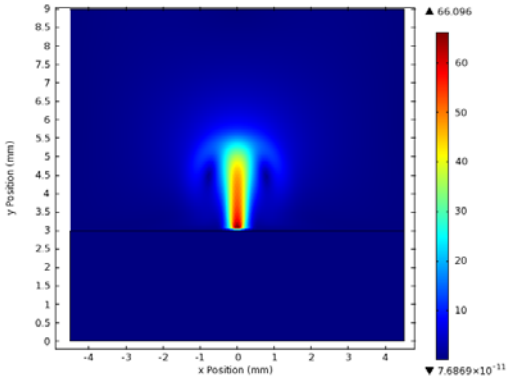

Figure 3. Velocity field at t=2 msec.

Movement within the melt pool begins to occur around this same time. Figure 4 shows the *x*-component (horizontal) of velocity at a point 10µm below the surface. The liquid iron moves in opposite directions on either side of the center of the optical beam. The velocity magnitude rises quickly over the next millisecond and is the

largest at those points at the ends of the melt pool.

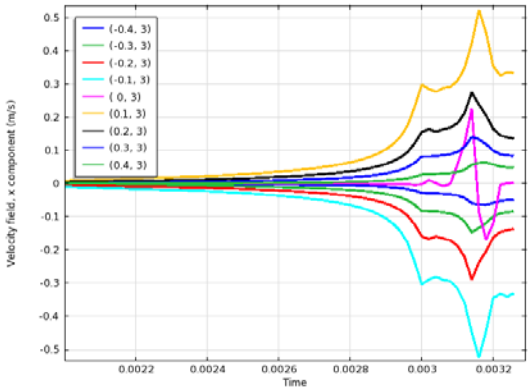

Figure 4. Horizontal velocity 10 µm inside the target

After a brief time, the vapor region expands horizontally and begins to affect a larger portion of the target surface. Figure 5 shows the y-component (vertical) at the same 10µm depth inside the target. The vertical velocity is highest in the center of the illumination zone and falls rapidly to the sides.

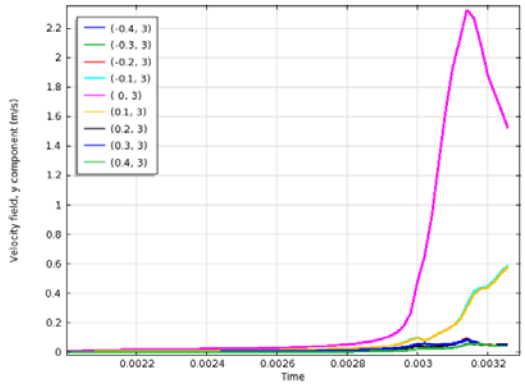

Figure 5. Vertical velocity 10 µm below the surface.

A particle trace is illustrated in Figure 6 which shows the flow history from a starting point 50µm beneath the surface of the iron from t=0 to 3.2msec.

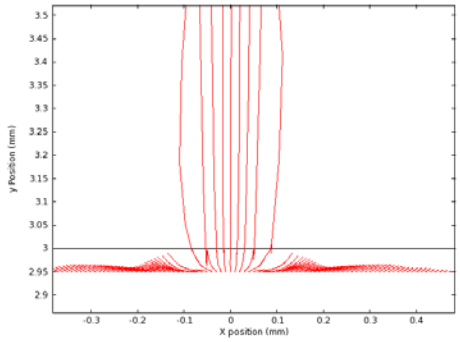

Figure 6. Particle trace from 50µm below the surface.

At t=3.2msec, the vaporized region expands to a significant portion of the illuminated area. Figure 7 identifies where the temperature is above the melting point of iron revealing a pool of liquefied iron to a depth of approximately 0.4mm. Likewise, Figure 8 shows where it is above vaporization illustrating a small area of vapor front progression into the target to a depth of about 50µm. This small region continues to advance and push liquid iron outward and upward as the early stage of hole formation begins.

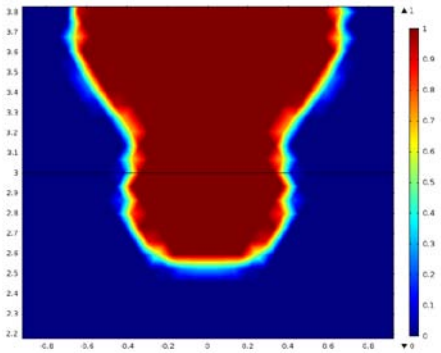

Figure 7. Region above melting.

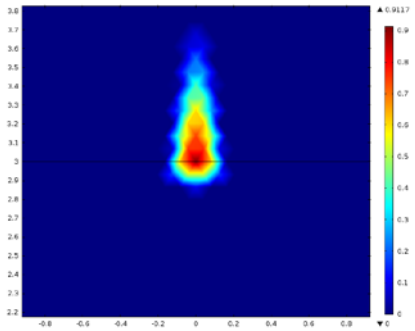

Figure 8. Region above vaporization.

5. Conclusions

This paper presents the results of a percussion laser drilling model using COMSOL Multiphysics® 4.3. The work focuses on the early stage of melt and vaporization using iron as the target material. Temperature dependent material properties are used to model the phase transitions that take place as the iron is heated from a solid-to-liquid and then to a gas. The velocity fields in the air above the target as well as the horizontal and vertical movement of liquid iron are investigated. A particle trace starting at 50 μm below the target's surface reveals details of the material flow pattern. The melt and vaporization regions at t=3.2msec show the size and shape of the vapor and melt fronts during early hole formation.

6. References

1. Ready, J. F., *Effect of High Power Laser Radiation*, Academic, London, UK, 1971.
2. Von Allmen, M., 'Laser Drilling Velocity in Metals,' *J. Appl. Phys*., **47**:5460, 1976.
3. Semak, V. & Matsunawa, A., 'The Role of Recoil Pressure in Energy Balance During Laser Materials Processing,' *J. Appl. Phys*. **30**:2541-2552, 1997.
4. Patel, R. S. & Brewster, M. Q., 'Gas- Assisted Laser-Metal Drilling: Theoretical Model,' *J. Thermophysics*, **5**(1):32-39, 1990.
5. Low, D.K.Y., Li, L. & Byrd, P.J., 'Hydrodynamic Analysis of Laser Drilling Process,' *ICALEO Conference Proceedings*, pp. 316-325, 2001.
6. Ng, G., Crouse, P., & Li, L., 'An Analytical Model for Laser Drilling Incorporating Effects of Exothermic Reaction, Pulse Width and Hole Geometry,' *Intl. J. Heat & Mass Trans*., **49**: 1358-1374, 2006.
7. Eppes, T., Milanovic, I. & Shetty, D., 'Laser Percussion Drilling Modeling Utility,' *J. Laser Appl*., **21**(2):102-109, 2009.